

Multi-wavelength magnetic coding of helical luminescence in ferromagnetic 2D layered CrI₃

Bo Peng^{1,2,*}, Zhiyong Chen^{1,2}, Yue Li^{1,2}, Zhen Liu^{1,2}, Difei Liang^{1,2,*}, Longjiang
Deng^{1,2}

¹National Engineering Research Center of Electromagnetic Radiation Control

Materials, School of Electronic Science and Engineering, University of Electronic
Science and Technology of China, Chengdu, 611731, China

²State Key Laboratory of Electronic Thin Films and Integrated Devices, University of
Electronic Science and Technology of China, Chengdu, 611731, China

*Correspondence author's e-mail: bo_peng@uestc.edu.cn; dfliang@uestc.edu.cn

Abstract: Two-dimensional (2D) van der Waals (vdW) ferromagnets have opened new avenues for manipulating spin at the limits of single or few atomic layers, and for creating unique magneto-exciton devices through the coupling of long-range ferromagnetic (FM) orders and excitons. However, 2D vdW ferromagnets explored so far have rarely possessed exciton behaviors; to date, FM CrI₃ have been recently revealed to show ligand-field photoluminescence correlated with FM ordering, but typically with a broad emission peak. Alternatively, many-body excitons have been observed in antiferromagnetic (AFM) NiPS₃, but the coupling of excitons with AFM orders is exponentially more difficult, owing to extremely high coercivity. Here, we report a straightforward approach to realize strong coupling of narrow helical emission and FM orders at a low magnetic field in CrI₃ through a relatively simple microsphere cavity. We show that the resonant whispering-gallery-modes (WGM) of SiO₂ microspheres give rising to a series of strong oscillation helical emissions with a full width at half-maximum (FWHM) of ~5 nm under continuous wave excitation. Reversible magnetic control and coding of helical luminescence with multiwavelength is realized in the range of 950-1100 nm. This work enables plenty of opportunities for creating magnetic encoding lasing for photonic integrated chips.

The emergence of long-range ferromagnetic orders in 2D vdW FM material has provided a new avenue for creating on-chip lasers, isolators and modulators for silicon photonics toward information processing and transmission through magneto-exciton coupling (Deng et al., 2018; Gong et al., 2017; Huang et al., 2017; Liu et al., 2021; Liu et al., 2020; Mak et al., 2019; Song et al., 2018; Sun et al., 2019). The magnetic orders can be switched between FM and AFM states by magnetic field (Klein et al., 2018; Zhong et al., 2017), electric gating (Huang et al., 2018; Jiang et al., 2018a; Jiang et al., 2018d; Zhang et al., 2020), electrostatic doping (Jiang et al., 2018b; Zheng et al., 2020) and hydrostatic pressure (Li et al., 2019; Song et al., 2019), which empower a pivotal foundation for realizing magnetic and electric control of magneto-optical coupling for information transfer. 2D vdW bilayer CrI_3 FM insulators used as spin valve in a magnetic tunneling junction device have highlighted flexibilities for encoding information and data storage (Jiang et al., 2018c; Klein et al., 2018; Song et al., 2018). To date, diverse 2D vdW FM and AFM metal, insulators and even semiconductors have been explored (Liu et al., 2021). FM $\text{Cr}_2\text{Ge}_2\text{Te}_6$ few-layer have demonstrated a p-type semiconducting behavior and gate-controllable magnetism (Jiang et al., 2018b; Verzhbitskiy et al., 2020); few-layer Fe_3GeTe_2 FM metal have shown high Curie temperature (T_c) above room temperature through ionic/protonic gating, patterning and interfacial exchange coupling (Deng et al., 2018; Li et al., 2018; May et al., 2019; Wang et al., 2020a); magnetic topological insulator MnBi_2Te_4 have recently been reported to present layer-dependent magnetic phase and spin-flop behaviors (Deng et al., 2020; Yang et al., 2021). Alternatively, air-stable metallic 2D vdW CrTe_2 and CrSe_2 with

thickness-dependent magnetic orders have been directly synthesized by chemical vapor deposition (CVD) methods (Li et al., 2021; Meng et al., 2021). However, thus far, few 2D vdW magnets have been revealed luminescence and exciton behaviors, and none examining magnetic coding of photoluminescence (PL), despite the discovery of luminescence in FM CrI₃ and AFM NiPS₃ (Hwangbo et al., 2021; Kang et al., 2020; Seyler et al., 2017; Wang et al., 2021). Moreover, the PL of CrI₃ derives from a ligand-field-allowed d-d transition, which naturally lead to a very broad PL peak with a FWHM of 100-200 nm owing to strong vibronic coupling (Seyler et al., 2017), extremely limiting the potential for photonic devices; in addition, it is difficult to achieve magnetic/electric control of spin in AFM NiPS₃, due to a high critical field up to 10 T at least (Wang et al., 2021).

With the rapid development of digitalization and semiconductor optoelectronics technology, various fields have an increasing demand for on-chip lasers, so the research on high-performance and miniaturized on-chip lasers is of great significance (Gao et al., 2020; Kyeremateng et al., 2017). On-chip lasers have broad application prospects, such as a light source for on-chip integrated photonic chips, laser scanning and ranging or flexible displays. Traditional directly modulated lasers (DML) have been achieved by injecting the pump current to the gain medium, and the modulation speed is affected by its volume of the active region and relaxation oscillation frequency (Dong et al., 2018; Kobayashi et al., 2013). Alternatively, topological lasers with single mode lasing and robustness against defects have been realized by coupling of photonic gain with topological structure (Bandres et al., 2018). Additionally, atomic-thin lasers using

transition-metal dichalcogenides (TMDs) with strong exciton emission as optical gain medium have been recently reported (Li et al., 2017; Salehzadeh et al., 2015a; Wu et al., 2015; Ye et al., 2015b). However, thus far, small-volume atomic-thin lasers with intrinsic magnetism in the near-infrared (NIR) region have been still elusive, which provide numerous opportunities to realized magnetic- field controlled DML. Moreover, the NIR laser is more challenging duo to the lack of gain medium with strong NIR emission.

Here, we report the realization of magnetic control and coding of NIR WGM emission through coupling of the luminescence of 2D ferromagnetic CrI₃ and SiO₂ microsphere cavities. Circularly polarized WGM PL features in CrI₃/microsphere are coupled with CrI₃ magnetic orders. The right-handed (left-handed) polarized WGM PL are dominated in a positive (negative) magnetic field of +1 T (-1 T). Multi-wavelength encoding is realized through repeatedly manipulating helicity of each WGM PL peak by magnetic field. This work opens the door to creating new atomically thin 2D magneto-optical devices for photonic integrated circuit and on-chip optical system.

Results

Coupling of magnetic orders and PL in CrI₃. In 2D FM CrI₃ monolayer, Cr³⁺ ions in each layer are coordinated by six nonmagnetic I⁻ ions to form an octahedron (Guo et al., 2020), which shares edges to build a honeycomb network (Fig. 1A). Monolayer CrI₃ is a Ising ferromagnetism arising from the Cr-I-Cr superexchange interaction, which is described by the Ising spin Hamiltonian, $H = -(1/2)\sum(J_{xy} S_{i(x)} S_{j(x)} + J_{xy} S_{i(y)} S_{j(y)} + J_z S_{i(z)} S_{j(z)})$, where $S_{i(x, y, z)}$ and $S_{j(x, y, z)}$ are the spin along the x, y, z direction of Cr³⁺ at $i(j)$ sites;

J_{xy} and J_z are the exchange coupling term of in-plane and out-of-plane spin components and $J_z > J_{xy} > 0$ in Ising FM model. In few-layer CrI_3 , intra-atomic $d-d$ transitions and charge-transfer transitions owing to ligand field lead to a broad layer-dependent PL emission at ~ 1020 nm with a FWHM of ~ 100 nm (Supplementary information, Fig. S1) (Seyler et al., 2017). PL intensities show strong layer dependence and significantly increase as increasing layers (Seyler et al., 2017), therefore, thick CrI_3 flakes and bulk were choose in our experiments. The helicity of the absorption and associated PL emission is correlated with the spin of the electrons at the ground states. Spin states are tied to magnetic orders of CrI_3 few-layers. Thus, in an out-of-plane positive magnetic field, the upper spin states are dominated and absorb right-hand polarized light, consequentially mostly giving right-hand polarized PL emission (Fig. 1B); when the magnetic field turns downward, the spins of electrons are reversed, and mainly lead to left-hand polarized PL (Supplementary information, Fig. S1). But the poor and broad PL features restrict the exploring on magneto-exciton coupling and creating photonic devices with unique functions. Optical microcavities have been widely applied to enhance light-matter interaction and suppress FWHM for realizing strong emission and lasing (Salehzadeh et al., 2015b; Schwarz et al., 2014; Wu et al., 2014; Ye et al., 2015a). SiO_2 microsphere as high-quality WGM microcavities with high Q-factor of $\sim 10^8$ can significantly enhance the coupling between gain medium and optical cavity modes (Mi et al., 2017; Zhao et al., 2018). Thus, SiO_2 microsphere cavities can be coupled with FM 2D layered CrI_3 to create narrow and strong WGM oscillation PL peaks. The coupling between circularly polarized PL emission and SiO_2 spherical microcavities

obey the law of conservation of angular momentum, thus, the PL helicity associated with magnetic orders are preserved. In a positive magnetic field, right-hand polarization-resolved WGM oscillation PL originating from spin-up states are dominated, and vice versa (Fig. 1C). Polarization-resolved Raman spectra show that thick layered CrI₃ bulk sample adopts a rhombohedral structure at 10 K. Raman shift of the two-fold degenerated E_g mode at $\sim 107\text{ cm}^{-1}$ are independent of the polarization angle (Fig. 2A and Fig. S2), validating the high-symmetry rhombohedral phase (Li et al., 2019; Song et al., 2019). Reflective magnetic circular dichroism (RMCD) was used to probe the long-range FM orders. A 633 nm continuous-wave laser was applied as an excitation source with the light spot size of $\sim 2\text{ }\mu\text{m}$ and 2 μW . Figure 2B and C show the typical RMCD curve of bare CrI₃ and CrI₃ beneath SiO₂ sphere. Striking hysteresis loops are observed on both bare CrI₃ and CrI₃ beneath SiO₂ sphere below 55 K, indicating a T_c of $\sim 50\text{ K}$ and the SiO₂ microsphere cavities do not influence the T_c of CrI₃.

Magnetic control of WGM PL emission of CrI₃. To obtain strong enhancements, SiO₂ microspheres with 10 and 12.5 μm diameter were transferred onto mechanically exfoliated thick CrI₃ flakes ($\sim 32\text{ nm}$) and bulk ($\sim 55\text{ nm}$) through polydimethylsiloxane (PDMS) films (Supplementary information, Fig. S2). The Q factors of SiO₂ spherical cavities were firstly estimated on MoS₂/SiO₂ samples. The Q factors of microsphere cavities are estimated from $Q=\lambda/\delta\lambda$, where $\delta\lambda$ is the FWHM of the WGMs, and the Q factor for the TM_{1,61} mode ($\sim 633\text{ nm}$) can reach about 1055 (supplementary information, Fig. S3). As shown in Figure S3B, the PL intensity increases sharply with

increasing excitation light power, and the lasing behavior at the $TM_{1,61}$ mode (~ 633 nm) is observed. Figure S3C shows that PL intensity of MoS_2/SiO_2 and MoS_2 as a function of laser power. The PL intensities of MoS_2 shows a linear dependence on the excitation light power, and $TM_{1,61}$ mode shows a kink indicating the onset of superlinear emission. In Figure S3D, the FWHM of $TM_{1,61}$ mode decreases from 0.9 to 0.6 nm, the linewidth narrowing effect further confirms the appearance of lasing. Room-temperature lasing from MoS_2 /sphere validate that Q-factor of SiO_2 is high enough for WGM lasing (Zhao et al., 2018). WGM PL peaks in the range of ~ 900 - 1100 nm are unambiguously observed from CrI_3 beneath 10 and 12.5 μm SiO_2 spheres under continuous wave 633 nm excitation with 1 mW (Supplementary information, Fig. S4). SiO_2 microsphere optical cavities enhance PL intensity of CrI_3 by ~ 2.7 times as compared to that from the same but bare CrI_3 . The excitation area can be effectively reduced to enhance the coupling between the gain region and the optical mode due to the lens effect of the microspheres (Mi et al., 2017; Zhao et al., 2018), which increases the spontaneous emission efficiency and PL intensity of CrI_3 . In stark contrast, no any oscillation peak is detected in bare CrI_3 sample. Theoretical calculations demonstrate that the strong WGM PL are attributed to the first-order TM modes (TM_1), as indicated by blue line (Supplementary information, Fig. S4).

To study the WGM PL in the microsphere cavity, power-dependent PL spectra were recorded on CrI_3 /microsphere vertical light-emitting gain structure in the range from 10 μW to 1.5 mW with a 633 nm laser excitation source at 10 K. The lensing and screening effects of the microsphere cavity increase the excitation efficiency of CrI_3 ,

the equally-spaced oscillation peaks can be distinguished, even the excitation power is as low as about 10 μ W (Supplementary information, Fig. S5 and S6). The WGM PL intensities linearly increase with laser power increasing. When the laser power is increased to 1.5 mW, the oscillation peaks intensity increases sharply and the peak width is narrowed. The spacing between two adjacent resonant modes remains constant with increasing laser power, indicating that the WGM PL originating from the same resonant modes of the sphere cavities. The PL intensities of bare CrI₃ samples also linearly increase with the increase of laser power, but smaller than WGM PL intensity. The integrated PL intensities of TM_{1,36}, TM_{1,37}, TM_{1,47} and TM_{1,48} modes of CrI₃/microsphere with 10 and 12.5 μ m SiO₂ spheres remains linear to the excitation power density. With further increasing laser power, the WGM oscillation peak intensity of the sample achieve maximum at 2.6 mW and drastically decrease at 3.0 mW due to laser burning of CrI₃ flakes. But no transition from spontaneous emission to amplified spontaneous emission was observed (Supplementary information, Fig. S5 and S6). This may be because the gain of CrI₃ flakes is not strong enough and they are also easy to burn out under high power, resulting in no super linear response. The PL intensity of thin CrI₃ was strongly dependent on the number of layers, and decrease with decreasing thickness of CrI₃. Even no WGM peaks are observed and only PL enhancement behaviors take place if the gain of CrI₃ is decreased by applying thin CrI₃ flakes (Supplementary information, Fig. S7). WGM PL features are nearly same in 10 and 12.5 μ m SiO₂ microsphere cavities. Therefore, we focus on 10 μ m SiO₂ microcavities to further study the magnetic control and coding of WGM PL.

WGM PL of CrI₃/microsphere can be manipulated by an out-of-plane magnetic field. Figure 3 presents the circularly polarization-resolved WGM PL features from CrI₃/microsphere at 10 K, at magnetic field +1, 0, -1 and 0 T, respectively. We define the right-hand (left-hand) circularly polarized PL spectra upon excitation by right-hand (left-hand) circularly polarized laser as RR (LL). The intensity of circularly polarized WGM PL is correlated to magnetic orders of CrI₃. In a magnetic field of +1 T, the FM orders are spin-up, leading to that the spin-up states are dominated, therefore, RR WGM PL is stronger than LL WGM PL (Fig. 3A and E). As the magnetic field is lowered to 0 T, the CrI₃ show an anti-ferromagnetic behavior, and spin-up and spin-down states are nearly equal (Fig. 3B and E). When magnetic field is further reversed to -1 T, spin states are also inversed, giving rise to opposite helicity and exhibiting a stronger LL component than RR (Fig. 3C and E). When magnetic field return back to 0 and +1 T, the WGM PL is also recovered (Fig. 3D and A). The corresponding RMCD results clearly show the associated FM and AFM orders, which consist with the magnetic control behaviors of circularly polarization-resolved WGM PL. It should be noted that the intensity variations of right-handed and left-handed polarized PL of the CrI₃/sphere are lower than the same pure CrI₃ flakes (Fig. 3 and supplementary information, Fig. S1). This probably results from the decrease of magnetic anisotropy and long-range ferromagnetic orders induced by tensile strains, which are formed during the transferring SiO₂ sphere onto CrI₃ by a PPMA fixed-point transfer method. Previous reports have demonstrated that tensile strains lead to an increase of bandgap associated with unchanged valence band maximum (VBM) and higher conduction band minimum

(CBM) (Webster and Yan, 2018; Zhang et al., 2015). Fig. S7B shows that the PL peak is blue-shifted to a high energy, which indicates that tensile strains are formed on CrI₃ flakes. Tensile strains lead to the increase of the Cr-I-Cr angle and bond length, which result in decreasing magnetic anisotropy energies and ferromagnetic orders of CrI₃. The helicity of PL emission of CrI₃ is strongly tied to magnetic orders. Therefore, the intensity variations of circularly polarized PL of CrI₃/sphere decrease.

Multiwavelength magnetic encoding. The WGM oscillation modes of sphere cavities result in a series of narrow PL at multiwavelength. We studied the multiwavelength magnetic encoding of circularly polarized PL through recycling a loop of magnetic field between +1 and -1 T. Magnetic field loop is set from +1 to 0 T and inversely increase to -1 T, and return back to +1 T (Fig. 4A). The PL intensity differences between LL and RR WGM PL, defined as ΔI , show striking narrow oscillation peaks at 976, 995, 1020, 1045 and 1070 nm with FWHM between 5 and 10 nm (Fig. 4B), which show an obvious magnetic-field dependent behavior. ΔI at the five distinct wavelengths are opposite at +1 and -1 T, and much larger than that at 0 T, which provide a rich platform for tri-state encoding through on/off switching of magnetic field. Figure 4b show ten recycling of ΔI for multiwavelength magnetic encoding. The ΔI features at 1020 ± 5 , 1070 ± 5 , 1045 ± 5 and 995 ± 5 nm were extracted. Each wavelength presents +1, 0 and -1 tri-states at magnetic field of +1, 0 and -1T. The magnetic control behaviors of tri-states are entirely correlated to the magnetic field and display the same shape with magnetic field setups, as shown in Fig. 4C and Fig. 5. The helicity of CrI₃/microsphere WGM oscillation peaks are determined by magnetic orders of CrI₃ and controlled by magnetic field,

which also can be used to achieve magnetic encoding function. Similar magnetic-field control behaviors have been achieved on different samples (Fig. 4B and Fig. 3), although the PL intensity variations is different, which strongly validate that the SiO₂ spherical cavities can generally lead to WGM peaks for CrI₃ ferromagnetism and reversible magnetic control and coding of helical luminescence in the CrI₃/microsphere is reproducible. The degree of polarization (DOP) from CrI₃/microsphere and CrI₃ is given by $DOP = (I_{RR} - I_{LL}) / (I_{LL} + I_{RR})$, where I_{RR} and I_{LL} are the intensity of right-hand and left-hand circularly polarized PL (Li et al., 2020; Peng et al., 2017; Wang et al., 2020b). When a magnetic field of +1 T is applied, DOP of the WGM PL is around +10%, while the DOP is inversely changed to -10% in a -1 T magnetic field, due to the reversal of the magnetization of CrI₃ (Fig. 6). Magnetic fields manipulate the DOP of each oscillation peak in ten recycling, clearly validating multiwavelength magnetic encoding behaviors.

Discussion

In summary, we demonstrated magnetic control of NIR helical WGM PL and realized tri-state encoding at different wavelength. The lensing and screening effects of SiO₂ microspheres increase the spontaneous emission efficiency of CrI₃ to create unambiguous WGM oscillation peaks which is coupled with magnetic orders of CrI₃. Magnetic fields manipulate and control each WGM peak, and the PL helicity and intensity difference of every WGM peak are applied to realize multiwavelength encoding through recycling magnetic fields. This work provides promising opportunities for creating magneto-optical devices and integrated photonic lasing with

magnetic encoding function through FM 2D materials microcavity.

Methods

Sample preparation.

CrI₃ flakes were mechanically exfoliated from bulk crystal onto polydimethylsiloxane films and then transferred onto SiO₂/Si substrates. The commercial SiO₂ microspheres solution were dropped onto another SiO₂/Si substrates, which were heated on a heating table to make the solvent completely volatilize. Next, SiO₂ microspheres were directly transferred onto CrI₃ flakes. The samples were loaded into cold head for optical measurements in glove box.

Optical measurements.

The Raman and PL signal were recorded by Witec Alpha 300R Plus confocal Raman microscope, coupled with a closed-cycle He optical cryostat (10 K) and a 7 T magnetic field. The excitation laser of 633 nm was 2 mW and the integration time was 15 s. A 633 nm HeNe laser with ~2 μ W was coupled to the Witec Raman system through free optical path for RMCD measurements, which was modulated by photoelastic modulator (PEM, $f_{PEM} = 50$ KHz) and focused onto samples by a long working distance 50 \times objective (NA = 0.45). The reflected beams were collected by the same objective, passed through a non-polarizing beamsplitter cube into an APD photodetector.

Data availability. All relevant data are available from the corresponding authors on request.

Reference

Bandres, M.A., Wittek, S., Harari, G., Parto, M., Ren, J., Segev, M., Christodoulides,

D.N., and Khajavikhan, M. (2018). Topological insulator laser: Experiments. *Science* 359 <http://dx.doi.org/10.1126/science.aar4005>.

Deng, Y., Yu, Y., Shi, M.Z., Guo, Z., Xu, Z., Wang, J., Chen, X.H., and Zhang, Y. (2020). Quantum anomalous Hall effect in intrinsic magnetic topological insulator MnBi_2Te_4 . *Science* 367, 895-900. <http://dx.doi.org/10.1126/science.aax8156>.

Deng, Y., Yu, Y., Song, Y., Zhang, J., Wang, N.Z., Sun, Z., Yi, Y., Wu, Y.Z., Wu, S., Zhu, J., et al. (2018). Gate-tunable room-temperature ferromagnetism in two-dimensional Fe_3GeTe_2 . *Nature* 563, 94-99. <http://dx.doi.org/10.1038/s41586-018-0626-9>.

Dong, P., Maho, A., Brenot, R., Chen, Y.-K., and Melikyan, A. (2018). Directly Reflectivity Modulated Laser. *Journal of Lightwave Technology* 36, 1255-1261. <http://dx.doi.org/10.1109/jlt.2018.2791363>.

Gao, Y., Lo, J.-C., Lee, S., Patel, R., Zhu, L., Nee, J., Tsou, D., Carney, R., and Sun, J. (2020). High-Power, Narrow-Linewidth, Miniaturized Silicon Photonic Tunable Laser With Accurate Frequency Control. *Journal of Lightwave Technology* 38, 265-271. <http://dx.doi.org/10.1109/jlt.2019.2940589>.

Gong, C., Li, L., Li, Z., Ji, H., Stern, A., Xia, Y., Cao, T., Bao, W., Wang, C., Wang, Y., et al. (2017). Discovery of intrinsic ferromagnetism in two-dimensional van der Waals crystals. *Nature* 546, 265–269. <http://dx.doi.org/10.1038/nature22060>.

Guo, K., Deng, B., Liu, Z., Gao, C., Shi, Z., Bi, L., Zhang, L., Lu, H., Zhou, P., Zhang, L., et al. (2020). Layer dependence of stacking order in nonencapsulated few-layer CrI_3 . *Sci China Mater* 63, 413-420. <http://dx.doi.org/10.1007/s40843-019-1214-y>.

Huang, B., Clark, G., Klein, D.R., MacNeill, D., Navarro-Moratalla, E., Seyler, K.L.,

Wilson, N., McGuire, M.A., Cobden, D.H., Xiao, D., et al. (2018). Electrical control of 2D magnetism in bilayer CrI₃. *Nat Nanotechnol* *13*, 544-548. <http://dx.doi.org/10.1038/s41565-018-0121-3>.

Huang, B., Clark, G., Navarro-Moratalla, E., Klein, D.R., Cheng, R., Seyler, K.L., Zhong, D., Schmidgall, E., McGuire, M.A., Cobden, D.H., et al. (2017). Layer-dependent ferromagnetism in a van der Waals crystal down to the monolayer limit. *Nature* *546*, 270-273. <http://dx.doi.org/10.1038/nature22391>.

Hwangbo, K., Zhang, Q., Jiang, Q., Wang, Y., Fonseca, J., Wang, C., Diederich, G.M., Gamelin, D.R., Xiao, D., Chu, J.-H., et al. (2021). Highly anisotropic excitons and multiple phonon bound states in a van der Waals antiferromagnetic insulator. *Nat Nanotechnol* *16*, 655-660. <http://dx.doi.org/10.1038/s41565-021-00873-9>.

Jiang, S., Li, L., Wang, Z., Mak, K.F., and Shan, J. (2018a). Controlling magnetism in 2D CrI₃ by electrostatic doping. *Nat Nanotechnol* *13*, 549-553. <http://dx.doi.org/10.1038/s41565-018-0135-x>.

Jiang, S., Li, L., Wang, Z., Mak, K.F., and Shan, J. (2018b). Controlling magnetism in 2D CrI₃ by electrostatic doping. *Nat Nanotechnol* *13*, 549-553. <http://dx.doi.org/10.1038/s41565-018-0135-x>.

Jiang, S., Li, L., Wang, Z., Mak, K.F., and Shan, J. (2018c). Controlling magnetism in 2D CrI₃ by electrostatic doping. *Nat Nanotechnol* *13*, 549-553. <http://dx.doi.org/10.1038/s41565-018-0135-x>.

Jiang, S., Shan, J., and Mak, K.F. (2018d). Electric-field switching of two-dimensional van der Waals magnets. *Nat Mater* *17*, 406-410 <http://dx.doi.org/10.1038/s41563-018->

0040-6.

Kang, S., Kim, K., Kim, B.H., Kim, J., Sim, K.I., Lee, J.-U., Lee, S., Park, K., Yun, S., Kim, T., et al. (2020). Coherent many-body exciton in van der Waals antiferromagnet NiPS₃. *Nature* 583, 785-789. <http://dx.doi.org/10.1038/s41586-020-2520-5>.

Klein, D.R., MacNeill, D., Lado, J.L., Soriano, D., Navarro-Moratalla, E., Watanabe, K., Taniguchi, T., Manni, S., Canfield, P., Fernández-Rossier, J., et al. (2018). Probing magnetism in 2D van der Waals crystalline insulators via electron tunneling. *Science* 360, 1218-1222. <http://dx.doi.org/10.1126/science.aar3617>.

Kobayashi, W., Ito, T., Yamanaka, T., Fujisawa, T., Shibata, Y., Kurosaki, T., Kohtoku, M., Tadokoro, T., and Sanjoh, H. (2013). 50-Gb/s Direct Modulation of a 1.3- μ m InGaAlAs-Based DFB Laser With a Ridge Waveguide Structure. *IEEE Journal of Selected Topics in Quantum Electronics* 19, 1500908-1500908. <http://dx.doi.org/10.1109/jstqe.2013.2238509>.

Kyeremateng, N.A., Brousse, T., and Pech, D. (2017). Microsupercapacitors as miniaturized energy-storage components for on-chip electronics. *Nat Nanotechnol* 12, 7-15. <http://dx.doi.org/10.1038/nnano.2016.196>.

Li, B., Wan, Z., Wang, C., Chen, P., Huang, B., Cheng, X., Qian, Q., Li, J., Zhang, Z., Sun, G., et al. (2021). Van der Waals epitaxial growth of air-stable CrSe₂ nanosheets with thickness-tunable magnetic order. *Nat Mater* <http://dx.doi.org/10.1038/s41563-021-00927-2>.

Li, Q., Yang, M., Gong, C., Chopdekar, R.V., N'Diaye, A.T., Turner, J., Chen, G., Scholl, A., Shafer, P., Arenholz, E., et al. (2018). Patterning-Induced Ferromagnetism of

Fe₃GeTe₂ van der Waals Materials beyond Room Temperature. *Nano Letters* *18*, 5974-5980. <http://dx.doi.org/10.1021/acs.nanolett.8b02806>.

Li, Q., Zhao, X., Deng, L., Shi, Z., Liu, S., Wei, Q., Zhang, L., Cheng, Y., Zhang, L., Lu, H., et al. (2020). Enhanced valley Zeeman splitting in Fe-doped monolayer MoS₂. *ACS Nano* *14*, 4636-4645. <http://dx.doi.org/10.1021/acsnano.0c00291>.

Li, T., Jiang, S., Sivadas, N., Wang, Z., Xu, Y., Weber, D., Goldberger, J.E., Watanabe, K., Taniguchi, T., Fennie, C.J., et al. (2019). Pressure-controlled interlayer magnetism in atomically thin CrI₃. *Nat Mater* *18*, 1303-1308. <http://dx.doi.org/10.1038/s41563-019-0506-1>.

Li, Y., Zhang, J., Huang, D., Sun, H., Fan, F., Feng, J., Wang, Z., and Ning, C.Z. (2017). Room-temperature continuous-wave lasing from monolayer molybdenum ditelluride integrated with a silicon nanobeam cavity. *Nat Nanotechnol* *12*, 987-992. <http://dx.doi.org/10.1038/nnano.2017.128>.

Liu, Z., Deng, L., and Peng, B. (2021). Ferromagnetic and ferroelectric two-dimensional materials for memory application. *Nano Res* *14*, 1802-1813. <http://dx.doi.org/10.1007/s12274-020-2860-3>.

Liu, Z., Guo, K., Hu, G., Shi, Z., Li, Y., Zhang, L., Chen, H., Zhang, L., Zhou, P., Lu, H., et al. (2020). Observation of nonreciprocal magnetophonon effect in nonencapsulated few-layered CrI₃. *Sci Adv* *6*, eabc7628. <http://dx.doi.org/10.1126/sciadv.abc7628>.

Mak, K.F., Shan, J., and Ralph, D.C. (2019). Probing and controlling magnetic states in 2D layered magnetic materials. *Nat Rev Phys* *1*, 646-661.

<http://dx.doi.org/10.1038/s42254-019-0110-y>.

May, A.F., Ovchinnikov, D., Zheng, Q., Hermann, R., Calder, S., Huang, B., Fei, Z., Liu, Y., Xu, X., and McGuire, M.A. (2019). Ferromagnetism Near Room Temperature in the Cleavable van der Waals Crystal Fe₅GeTe₂. *ACS Nano* *13*, 4436-4442. <http://dx.doi.org/10.1021/acsnano.8b09660>.

Meng, L., Zhou, Z., Xu, M., Yang, S., Si, K., Liu, L., Wang, X., Jiang, H., Li, B., Qin, P., et al. (2021). Anomalous thickness dependence of Curie temperature in air-stable two-dimensional ferromagnetic 1T-CrTe₂ grown by chemical vapor deposition. *Nat Commun* *12*, 809. <http://dx.doi.org/10.1038/s41467-021-21072-z>.

Mi, Y., Zhang, Z., Zhao, L., Zhang, S., Chen, J., Ji, Q., Shi, J., Zhou, X., Wang, R., Shi, J., et al. (2017). Tuning excitonic properties of monolayer MoS₂ with microsphere cavity by high-throughput chemical vapor deposition method. *Small* *13*, 1701694. <http://dx.doi.org/10.1002/sml.201701694>.

Peng, B., Li, Q., Liang, X., Song, P., Li, J., He, K., Fu, D., Li, Y., Shen, C., Wang, H., et al. (2017). Valley polarization of trions and magnetoresistance in heterostructures of MoS₂ and yttrium iron garnet. *ACS Nano* *11*, 12257-12265. <http://dx.doi.org/10.1021/acsnano.7b05743>.

Salehzadeh, O., Djavid, M., Tran, N.H., Shih, I., and Mi, Z. (2015a). Optically Pumped Two-Dimensional MoS₂ Lasers Operating at Room-Temperature. *Nano Lett* *15*, 5302-5306. <http://dx.doi.org/10.1021/acs.nanolett.5b01665>.

Salehzadeh, O., Djavid, M., Tran, N.H., Shih, I., and Mi, Z. (2015b). Optically Pumped Two-Dimensional MoS₂ Lasers Operating at Room-Temperature. *Nano Lett* *15*, 5302-

5306. <http://dx.doi.org/10.1021/acs.nanolett.5b01665>.

Schwarz, S., Dufferwiel, S., Walker, P.M., Withers, F., Trichet, A.A.P., Sich, M., Li, F., Chekhovich, E.A., Borisenko, D.N., Kolesnikov, N.N., et al. (2014). Two-dimensional metal-chalcogenide films in tunable optical microcavities. *Nano Lett* *14*, 7003-7008. <http://dx.doi.org/10.1021/nl503312x>.

Seyler, K.L., Zhong, D., Klein, D.R., Gao, S., Zhang, X., Huang, B., Navarro-Moratalla, E., Yang, L., Cobden, D.H., McGuire, M.A., et al. (2017). Ligand-field helical luminescence in a 2D ferromagnetic insulator. *Nature Physics* *14*, 277-281. <http://dx.doi.org/10.1038/s41567-017-0006-7>.

Song, T., Cai, X., Tu, M.W.-Y., Zhang, X., Huang, B., Wilson, N.P., Seyler, K.L., Zhu, L., Taniguchi, T., Watanabe, K., et al. (2018). Giant tunneling magnetoresistance in spin-filter van der Waals heterostructures. *Science* *360*, 1214-1218. <http://dx.doi.org/10.1126/science.aar4851>.

Song, T., Fei, Z., Yankowitz, M., Lin, Z., Jiang, Q., Hwangbo, K., Zhang, Q., Sun, B., Taniguchi, T., Watanabe, K., et al. (2019). Switching 2D magnetic states via pressure tuning of layer stacking. *Nat Mater* *18*, 1298-1302. <http://dx.doi.org/10.1038/s41563-019-0505-2>.

Sun, Z., Yi, Y., Song, T., Clark, G., Huang, B., Shan, Y., Wu, S., Huang, D., Gao, C., Chen, Z., et al. (2019). Giant nonreciprocal second-harmonic generation from antiferromagnetic bilayer CrI₃. *Nature* *572*, 497-501. <http://dx.doi.org/10.1038/s41586-019-1445-3>.

Verzhbitskiy, I.A., Kurebayashi, H., Cheng, H., Zhou, J., Khan, S., Feng, Y.P., and Eda,

G. (2020). Controlling the magnetic anisotropy in $\text{Cr}_2\text{Ge}_2\text{Te}_6$ by electrostatic gating. *Nat Electron* 3, 460-465. <http://dx.doi.org/10.1038/s41928-020-0427-7>.

Wang, H., Liu, Y., Wu, P., Hou, W., Jiang, Y., Li, X., Pandey, C., Chen, D., Yang, Q., Wang, H., et al. (2020a). Above Room-Temperature Ferromagnetism in Wafer-Scale Two-Dimensional van der Waals Fe_3GeTe_2 Tailored by a Topological Insulator. *ACS Nano* 14, 10045-10053. <http://dx.doi.org/10.1021/acsnano.0c03152>.

Wang, X., Cao, J., Lu, Z., Cohen, A., Kitadai, H., Li, T., Tan, Q., Wilson, M., Lui, C.H., Smirnov, D., et al. (2021). Spin-induced linear polarization of photoluminescence in antiferromagnetic van der Waals crystals. *Nat Mater* <http://dx.doi.org/10.1038/s41563-021-00968-7>.

Wang, Y., Deng, L., Wei, Q., Wan, Y., Liu, Z., Lu, X., Li, Y., Bi, L., Zhang, L., Lu, H., et al. (2020b). Spin-valley locking effect in defect states of monolayer MoS_2 . *Nano Lett* 20, 2129-2136. <http://dx.doi.org/10.1021/acs.nanolett.0c00138>.

Webster, L., and Yan, J.-A. (2018). Strain-tunable magnetic anisotropy in monolayer CrCl_3 , CrBr_3 , and CrI_3 . *Physical Review B* 98 <http://dx.doi.org/10.1103/PhysRevB.98.144411>.

Wu, S., Buckley, S., Jones, A.M., Ross, J.S., Ghimire, N.J., Yan, J., Mandrus, D.G., Yao, W., Hatami, F., Vučković, J., et al. (2014). Control of two-dimensional excitonic light emission via photonic crystal. *2D Mater* 1, 011001. <http://dx.doi.org/10.1088/2053-1583/1/1/011001>.

Wu, S., Buckley, S., Schaibley, J.R., Feng, L., Yan, J., Mandrus, D.G., Hatami, F., Yao, W., Vuckovic, J., Majumdar, A., et al. (2015). Monolayer semiconductor nanocavity

lasers with ultralow thresholds. *Nature* **520**, 69-72.

<http://dx.doi.org/10.1038/nature14290>.

Yang, S., Xu, X., Zhu, Y., Niu, R., Xu, C., Peng, Y., Cheng, X., Jia, X., Huang, Y., Xu, X., et al. (2021). Odd-Even Layer-Number Effect and Layer-Dependent Magnetic Phase Diagrams in MnBi_2Te_4 . *Phys Rev X* **11**, 011003.

<http://dx.doi.org/10.1103/PhysRevX.11.011003>.

Ye, Y., Wong, Z.J., Lu, X., Ni, X., Zhu, H., Chen, X., Wang, Y., and Zhang, X. (2015a).

Monolayer excitonic laser. *Nat Photonics* **9**, 733-737.

<http://dx.doi.org/10.1038/nphoton.2015.197>.

Ye, Y., Wong, Z.J., Lu, X., Ni, X., Zhu, H., Chen, X., Wang, Y., and Zhang, X. (2015b).

Monolayer excitonic laser. *Nature Photonics* **9**, 733-737.

<http://dx.doi.org/10.1038/nphoton.2015.197>.

Zhang, W.-B., Qu, Q., Zhu, P., and Lam, C.-H. (2015). Robust intrinsic ferromagnetism and half semiconductivity in stable two-dimensional single-layer chromium trihalides.

Journal of Materials Chemistry C **3**, 12457-12468.

<http://dx.doi.org/10.1039/c5tc02840j>.

Zhang, X.-X., Li, L., Weber, D., Goldberger, J., Mak, K.F., and Shan, J. (2020). Gate-tunable spin waves in antiferromagnetic atomic bilayers. *Nat Mater* **19**, 838-842.

<http://dx.doi.org/10.1038/s41563-020-0713-9>.

Zhao, L., Shang, Q., Gao, Y., Shi, J., Liu, Z., Chen, J., Mi, Y., Yang, P., Zhang, Z., Du, W., et al. (2018). High-temperature continuous-wave pumped lasing from large-area monolayer semiconductors grown by chemical vapor deposition. *ACS Nano* **12**, 9390-

9396. <http://dx.doi.org/10.1021/acsnano.8b04511>.

Zheng, G., Xie, W.-Q., Albarakati, S., Algarni, M., Tan, C., Wang, Y., Peng, J., Partridge, J., Farrar, L., Yi, J., et al. (2020). Gate-Tuned Interlayer Coupling in van der Waals Ferromagnet Fe_3GeTe_2 Nanoflakes. *Phys Rev Lett* *125*, 047202. <http://dx.doi.org/10.1103/PhysRevLett.125.047202>.

Zhong, D., Seyler, K.L., Linpeng, X., Cheng, R., Sivadas, N., Huang, B., Schmidgall, E., Taniguchi, T., Watanabe, K., McGuire, M.A., et al. (2017). Van der Waals engineering of ferromagnetic semiconductor heterostructures for spin and valleytronics. *Sci Adv* *3*, e1603113. <http://dx.doi.org/10.1126/sciadv.1603113>.

Acknowledgements

We acknowledge financial support from National Natural Science Foundation of China (51872039, 52021001), Science and Technology Program of Sichuan (M112018JY0025).

Author contributions

B.P. developed the concept, designed the experiment. B.P., Z.Y.C, L.J.D, D.F.L prepared the manuscript and discussed the mechanism of magnetic encoding. Z.Y.C, Z.L. prepared the samples and performed the PL and Raman measurements. Y.L., contributed to fully relativistic calculations.

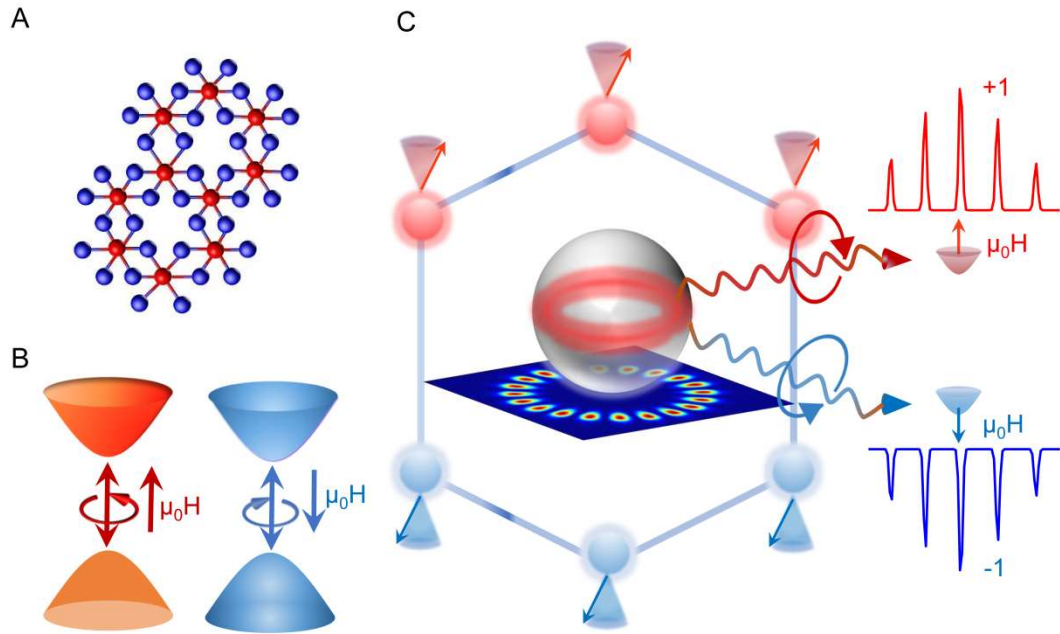


Fig. 1 CrI₃/microsphere WGM microcavities. (A) Atomic structure of monolayer CrI₃. Red and blue balls represent Cr and I atoms, respectively. (B) Schematic of magnetic control of right-hand (red) and left-hand (blue) circularly polarized PL light. (C) Magnetic encoding of WGM PL in CrI₃/microsphere cavities. Strong WGM oscillations lead to narrow circularly polarized WGM PL associated with magnetic orders upon excitation by circular polarization-resolved light.

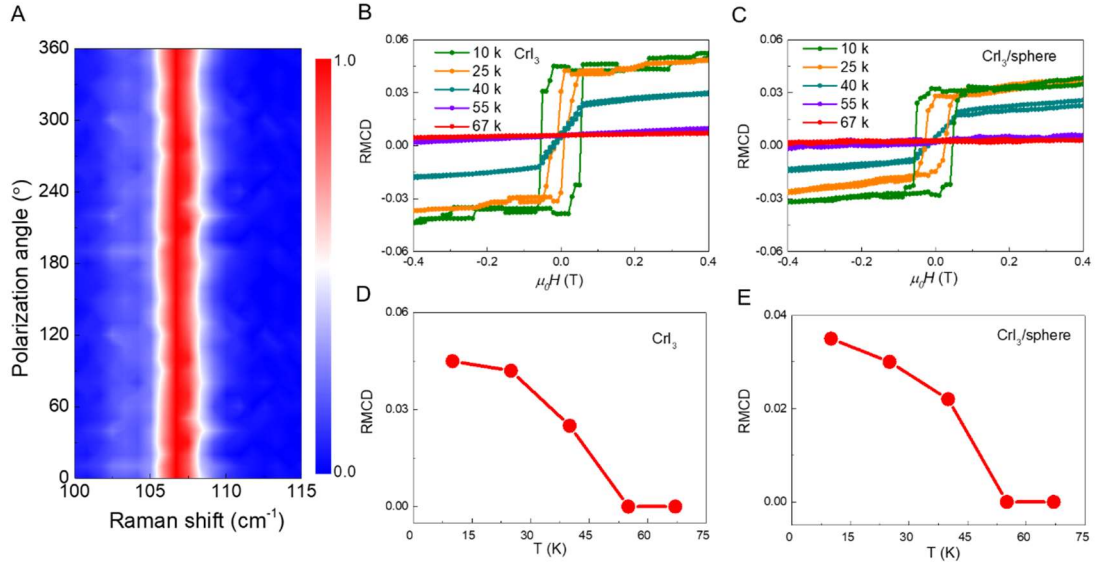


Fig. 2 Polarization-dependent Raman and RMCD measurements of CrI_3 /microsphere and bare CrI_3 . (A) Polarization angle dependent Raman maps of the CrI_3 bulk beneath a $10\ \mu\text{m}$ SiO_2 microsphere. (B, C) Temperature-dependent RMCD measurements of the bare CrI_3 and CrI_3 /microsphere ($10\ \mu\text{m}$). (D, E) Extracted RMCD intensities as a function of temperature from (B, C), showing a T_c of $\sim 50\ \text{K}$.

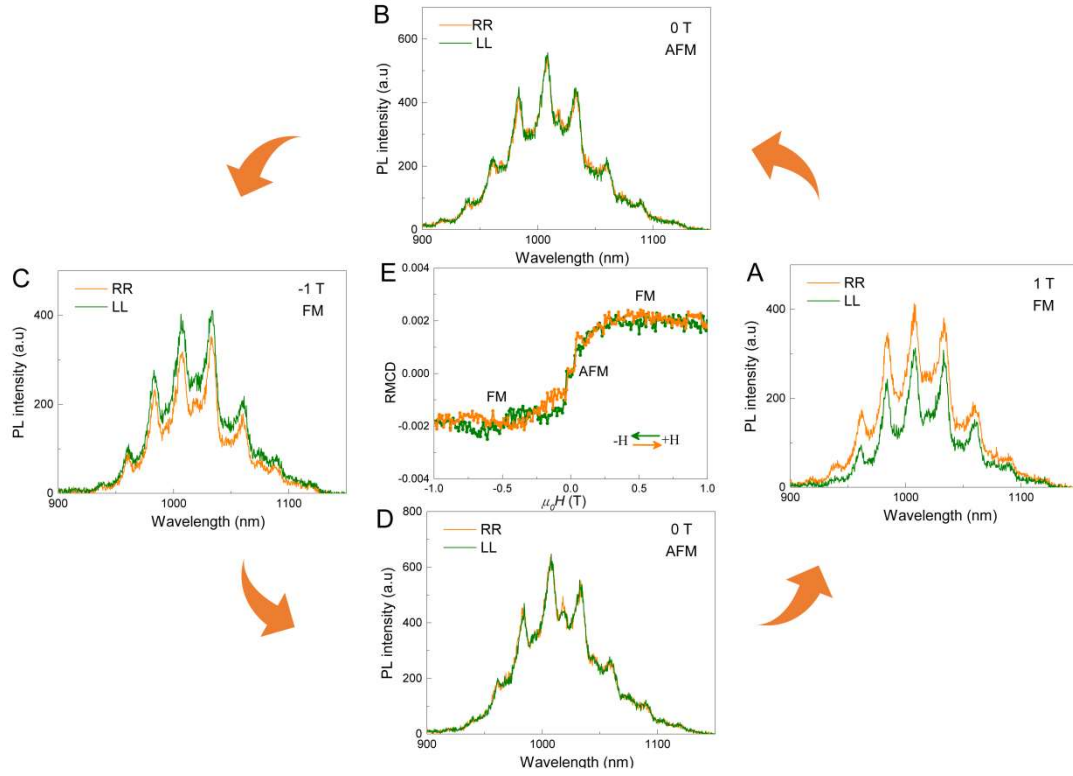


Fig. 3 Magnetic control of WGM PL of CrI₃ beneath a 10 μm SiO₂ microsphere.

(A-D) Circularly polarized PL spectra upon 2 mW 633 nm excitation with magnetic field at +1, 0, -1 and 0 T. (E) Corresponding RMCD curve as a function of magnetic field, which is consistent with the magnetic control of WGM PL.

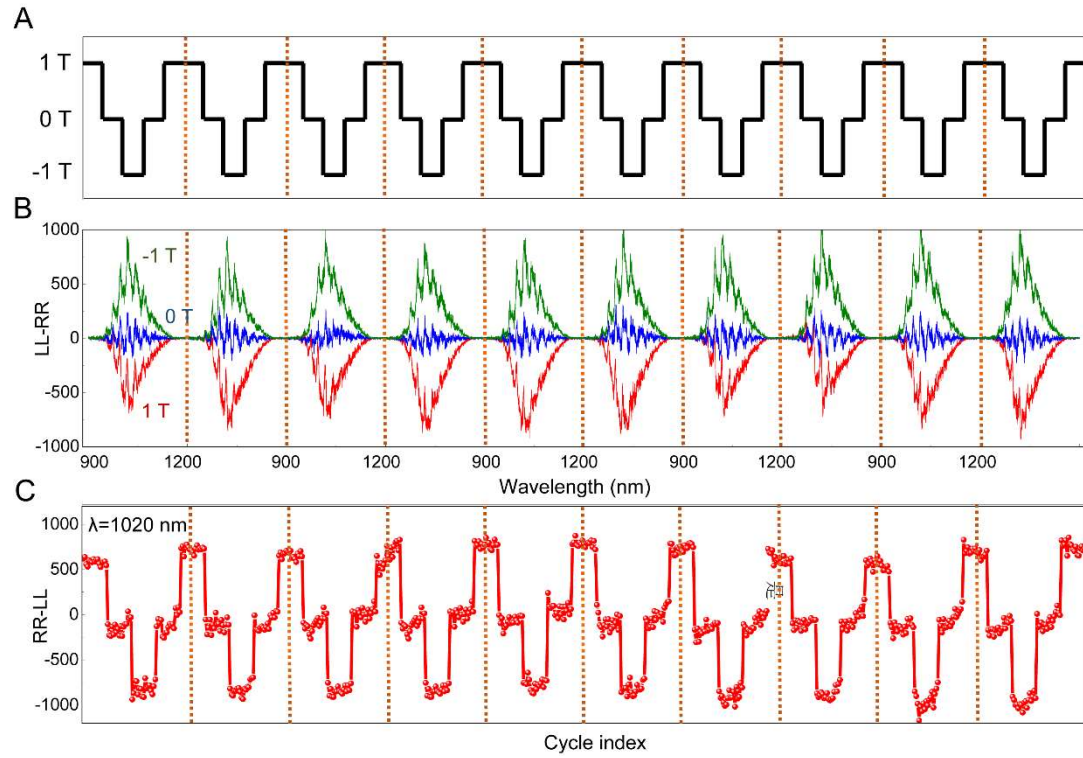


Fig. 4 Reversible magnetic control and coding of helical luminescence in the CrI₃/microsphere. (A) Schematic of the cycle-dependent magnetic field setup with a sequence of 1 T, 0 T, -1 T, 0 T and 1 T. (B) Recycling control of PL intensity difference between helical WGM PL of CrI₃/microsphere upon 2 mW 633 nm excitation by magnetic field. (C) Magnetic control and tri-state coding of WGM PL peaks at 1020 nm extracted from Fig. 4B.

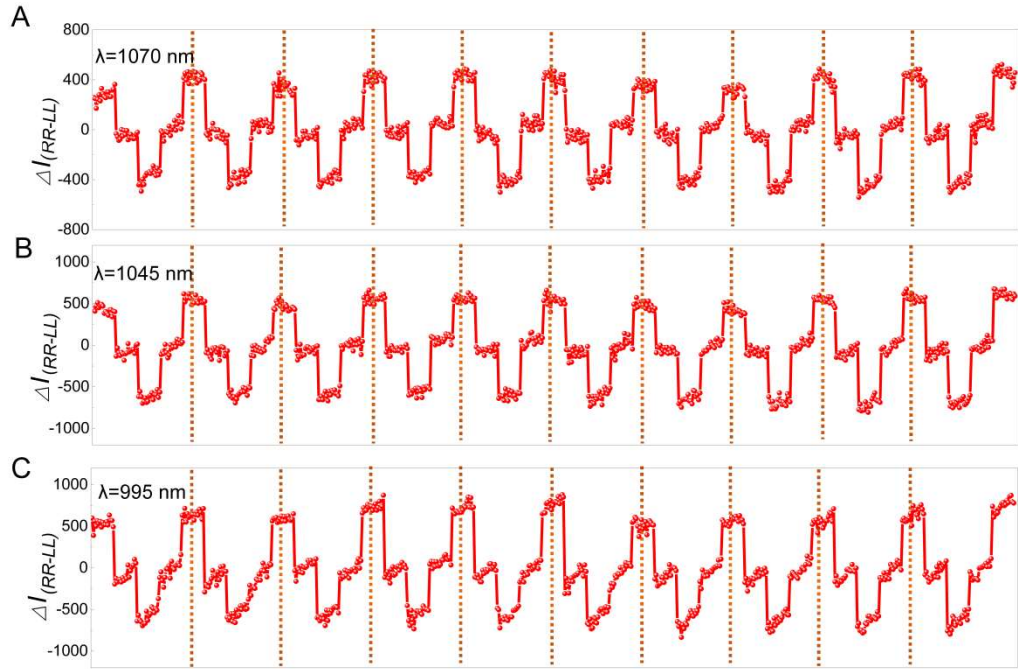


Fig.5 Multiwavelength magnetic coding through PL intensity difference of helical WGM luminescence. (A-C) Reversible magnetic control and tri-state coding at 1070, 1045 and 995 nm in selected magnetic fields of +1, 0, -1 T.

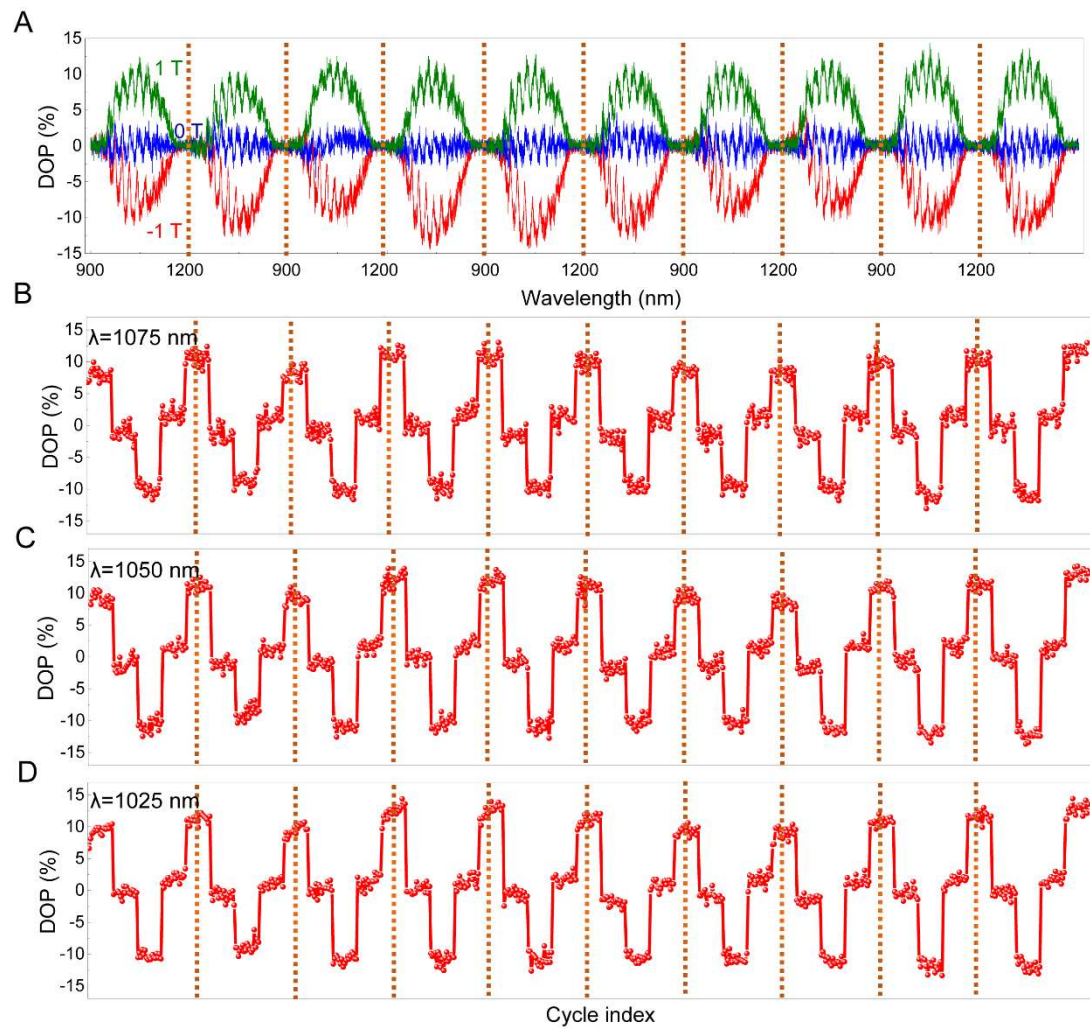


Fig.6 Multiwavelength magnetic coding through helicity of WGM luminescence. b

(A) Recycling magnetic control of DOP. (B-D) Corresponding tri-state magnetic encoding of DOP at 1075, 1050 and 1025 nm in selected magnetic fields of +1, 0, -1 T.